

ORGANIC CHEMISTRY OF LOW-MASS STAR-FORMING CORES I: 7 MM SPECTROSCOPY OF CHAMAELEON MMS1

MARTIN A. CORDINER¹, STEVEN B. CHARNLEY, EVA S. WIRSTRÖM¹

Astrochemistry Laboratory and The Goddard Center for Astrobiology, Mailstop 691, NASA Goddard Space Flight Center, 8800 Greenbelt Road, Greenbelt, MD 20770, USA

AND

ROBERT G. SMITH

School of Physical, Environmental & Mathematical Sciences, The University of New South Wales, Australian Defence Force Academy, Canberra ACT 2600, Australia

ApJ, in press

ABSTRACT

Observations are presented of emission lines from organic molecules at frequencies 32 – 50 GHz in the vicinity of Chamaeleon MMS1. This chemically-rich dense cloud core harbours an extremely young, very low-luminosity protostellar object and is a candidate first hydrostatic core. Column densities are derived and emission maps are presented for species including polyynes, cyanopolyynes, sulphuretted carbon-chains and methanol. The polyyne emission peak lies about 5000 AU from the protostar, whereas methanol peaks about 15,000 AU away. Averaged over the telescope beam, the molecular hydrogen number density is calculated to be 10^6 cm^{-3} and the gas kinetic temperature is in the range 5 – 7 K. The abundances of long carbon chains are very large, and are indicative of a non-equilibrium carbon chemistry; C_6H and HC_7N column densities are $5.9^{+2.9}_{-1.3} \times 10^{11} \text{ cm}^{-2}$ and $3.3^{+8.0}_{-1.5} \times 10^{12} \text{ cm}^{-2}$, respectively, which are similar to the values found in the most carbon-chain-rich protostars and prestellar cores known, and are unusually large for star-forming gas. Column density upper limits were obtained for the carbon-chain anions C_4H^- and C_6H^- , with anion-to-neutral ratios $[\text{C}_4\text{H}^-]/[\text{C}_4\text{H}] < 0.02\%$ and $[\text{C}_6\text{H}^-]/[\text{C}_6\text{H}] < 10\%$, consistent with previous observations in interstellar clouds and low-mass protostars. Deuterated HC_3N and *c*- C_3H_2 were detected. The $[\text{DC}_3\text{N}]/[\text{HC}_3\text{N}]$ ratio of approximately 4% is consistent with the value typically found in cold interstellar gas.

Subject headings: Astrochemistry – Stars: formation – ISM: abundances – Radio lines: ISM, stars

1. INTRODUCTION

During the earliest stages of star formation, quiescent molecular gas collapses to form a dense, prestellar core and subsequently a protostar with accretion disk, from which planetary systems may eventually arise. Understanding the evolution of molecular complexity as matter passes through these phases is crucial to the development of theories concerning organic chemistry during the formation of planetary systems, with relevance to the origin of life in the Galaxy (Ehrenfreund & Charnley 2000). Interstellar clouds and prestellar cores have been shown to host a rich organic chemistry that results in the synthesis of a range of large organic molecules (Herbst & van Dishoeck 2009). Unsaturated carbon-chain-bearing species such as the polyynes and cyanopolyynes are highly abundant in dark interstellar clouds such as TMC-1 (*e.g.* Cernicharo et al. 1984), and have recently been found to be present in large concentrations around some prestellar cores and low-mass protostars (Sakai et al. 2008b, 2009a; Gupta et al. 2009; Cordiner et al. 2011). It has been hypothesised that such complex molecules may survive the passage from protostellar envelope to accretion disk, to later become incorporated, largely unmodified, into solar system bodies such as comets (*e.g.* Meier et al. 1998; Willacy 2007; Charnley & Rodgers 2008, 2009; Mumma & Charnley 2011). Further observational and theoretical studies of the chemical evolution of gas and dust in the vicinity of protostars as they form and heat their surroundings will be crucial in order to

understand the chemical reagents present at the start of planet formation, and those delivered to planetary surfaces later by cometary impacts.

Chamaeleon MMS1 (abbreviated Cha-MMS1) is an ideal source in which to study the chemistry of a protostar in its natal environment. Thus far, Cha-MMS1 has been relatively little-studied in terms of its molecular inventory. It was first detected in 1.3 mm emission as a very compact object ($\approx 30''$ in diameter) by Reipurth et al. (1996). Infrared and sub-mm photometry are consistent with the presence of a young Class 0 protostar embedded in a dusty envelope with a core density of $3.3 \times 10^6 \text{ cm}^{-3}$ and diameter of about 3600 AU (Belloche et al. 2006). The central object has been classified by Belloche et al. (2006, 2011) as either an extremely young, very low-luminosity Class 0 protostar (VeLLO) or an example of a first hydrostatic core (FHSC). VeLLOs are likely to be young protostars undergoing episodic accretion, and a number of these were identified by the recent Spitzer c2d survey (Dunham et al. 2008). The FHSC is a transient, quasi-hydrostatic object predicted by the simulations of Larson (1969), but so far eluding observational confirmation. It is theorised to be formed in the early stages of protostellar collapse at the point when the density becomes sufficiently high that the core is opaque to thermal radiation. Virial heating then provides the energy to pressurise the (predominantly molecular hydrogen) gas against further collapse. Representative of a phase of protostar evolution preceding Class 0, the FHSC is also known as Class –I (Boss & Yorke 1995). The physics and chemistry of FHSCs and VeLLOs have recently been discussed by Omukai (2007) and Lee (2007), respectively. The predicted

martin.cordiner@nasa.gov

¹ Department of Physics, The Catholic University of America, Washington, DC 20064, USA

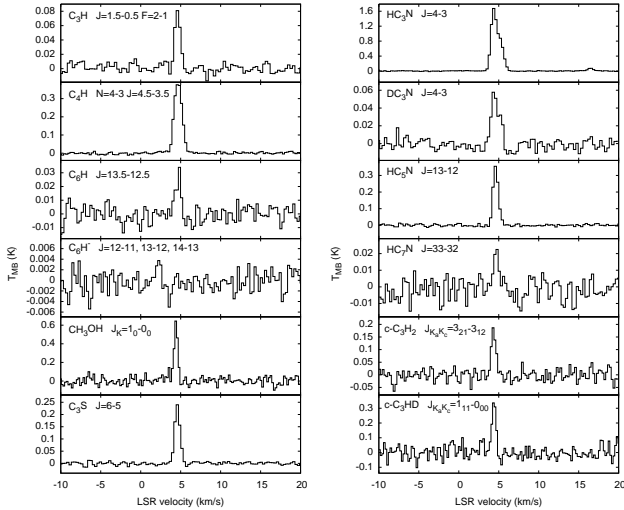


Fig. 1.— Example 7 mm Mopra spectra of Cha-MMS1. For C_6H^- , the spectrum shown is the average of the three observed lines.

spectral energy distribution of an FHSC is similar to that of the coolest, lowest-luminosity VeLLOs, and at present there are only four likely candidate FHSCs reported in the literature: Cha-MMS1, L1448 IRS2E (Chen et al. 2010), Per-Bolo 58 (Enoch et al. 2010) and L1451-mm (Pineda et al. 2011).

Observations of organic molecules in Cha-MMS1 were made previously by Kontinen et al. (2000) using SEST; Bellocche et al. (2006) observed a selection of deuterated and undeuterated molecular ions, and Tennekes et al. (2006) mapped the HCN and HNC emission around the protostar. However, the chemical and physical characterisation of Cha-MMS1 is still far from complete. As part of a program to understand organic chemistry during the earliest phases of low-mass star formation, we have initiated molecular line surveys in a sample of around 70 young protostars, focussing on individual sources for more detailed followup. In this article, we present 7 mm spectral line data and maps of cold carbon-chain-bearing species and other organic molecules in the vicinity of Cha-MMS1. These observations are analysed in the context of the physical and chemical properties of the protostellar envelope which, compared with other young carbon-chain-rich protostars (such as L1527 and L1521F, whose organic chemistry were recently examined by Sakai et al. 2008b and Takakuwa et al. 2011), help to constrain the current state and the history of the core.

2. OBSERVATIONS

Observations of Cha-MMS1 were carried out in March 2010 using the ATNF Mopra 22 m radio telescope. The Mopra Spectrometer (MOPS) was configured in zoom mode to simultaneously observe 16 spectral windows distributed over an 8 GHz range, each with a bandwidth of 137.5 MHz and a channel spacing of 33.6 kHz. During observations, the total system temperatures were in the range 80 – 200 K. The beam efficiency factor at 7 mm (42 GHz) was 0.6. Pointing was checked about every three hours and was typically accurate to within 5 – 10".

Position-switched integrations of Cha-MMS1 were performed at the (Kontinen et al. 2000) peak HC_3N position, at (J2000) coordinates R.A. = 11:06:33, decl. = -77:23:46. The off position used was R.A. = 11:17:38, decl. = -77:23:25. To help mitigate the known Mopra 30 MHz spectral baseline rip-

ple, the telescope subreflector was continuously driven up and down during observations, with a displacement of 3.5 mm. Atmospheric opacity corrections e^{τ_θ} are required at 7 mm; zenith optical depths as a function of frequency ($\tau_0(\nu)$) were calculated using the GILDAS ATM routine² based on the precipitable water vapour column and atmospheric temperature and pressure at the time of observations.

Observations were performed using two different MOPS configurations centered at frequencies of 36 GHz and 45 GHz, respectively. Approximately 22 hr of on-source integration was obtained for the 36 GHz setting, yielding RMS main-beam brightness temperature sensitivities $T_{MB}(RMS) \approx 6$ mK per channel. Two hours integration in the 45 GHz setting yielded $T_{MB}(RMS) \approx 30$ mK per channel. The observed molecular transition lines are given in Table 1. The telescope beam FWHM was 96" at 36 GHz and 77" at 45 GHz.

On-the-fly mapping of the $8' \times 8'$ region surrounding Cha-MMS1 was performed using the 36 GHz setting, employing a Nyquist sampling rate in the R.A. (scan) direction and 33" spacing between map rows. The resulting map sensitivity was $T_{MB}(RMS) \approx 70$ mK per channel per pixel.

Spectral line data were reduced and combined using standard routines in the ATNF Spectral Analysis Package (ASAP) version 3.0. Baseline subtraction and spectral line analysis were performed using NRAO IRAF³. Examples of a selection of the observed spectral lines are shown in Figure 1. Map data were reduced using the AIPS++ programs LIVEDATA and GRIDZILLA (see Barnes et al. 2001), and smoothed with a Gaussian FWHM of 96" applicable to the beam size at 36 GHz.

3. RESULTS

3.1. Molecular emission maps

Maps of the integrated line intensity $\int T_A d\nu$ are shown for HC_3N , HC_5N , C_4H , CH_3OH , CCS and C_3S in Figures 2 to 4. All mapped species show resolved structure with strong emission peaks within 2' of the protostar (which is plotted as an asterisk). The polyne-based species HC_3N , HC_5N and C_4H all show peaks that are approximately spatially coincident with each other and are elongated in the east-west direction. The sulphuretted carbon chains show a similar morphology, but are offset by about 35" to the west of the polyynes. Elliptical Gaussian fits to these carbon-chain-bearing species have FWHM $\sim 200'' \times 400''$, with the long axis orientated at a mean position angle -5° from the horizontal (E-W) axis. The methanol peak has similar dimensions, but is located 70" south-west of the polyne peak. Extended structures are present in all the carbon chain maps, the principal common feature being a ridge in the east-west direction, the full extent of which cannot be determined from our maps. The methanol distribution is markedly different however, with relatively little extension to the east of the protostar, and a secondary peak to the north-east. The polyne-based species peak closest to the protostar (about 30 – 40" away), followed by the sulphuretted carbon chains (60" away), then methanol (100" away). Assuming a distance to Cha-MMS1 of 150 pc (Knude & Hog 1998), these correspond to respective distances from the protostar of about 5,000 AU, 9,000 AU and 15,000 AU

² <http://www.iram.fr/IRAMFR/GILDAS>

³ IRAF is distributed by the National Optical Astronomy Observatory, which is operated by the Association of Universities for Research in Astronomy (AURA) under cooperative agreement with the National Science Foundation.

TABLE 1
OBSERVED LINE PARAMETERS

Species	Transition	Freq. (MHz)	T_{MB} (mK)	v_{LSR} (km s ⁻¹)	Δv (km s ⁻¹)	$\int T_{\text{MB}} dv$ (mK km s ⁻¹)
C ₆ H	² Π _{3/2} $J = 23/2 - 21/2 f$	31881.8596	17 (7)	4.71 (15)	0.93 (34)	17 (6)
C ₆ H	² Π _{3/2} $J = 23/2 - 21/2 e$	31885.5414	21 (6)	4.58 (13)	1.08 (31)	25 (7)
C ₃ H	$J = 3/2 - 1/2 e F = 2 - 1$	32660.6550	86 (10)	4.75 (2)	0.78 (6)	72 (8)
C ₃ H	$J = 3/2 - 1/2 e F = 1 - 0$	32663.3750	39 (7)	4.86 (5)	0.79 (14)	32 (6)
C ₃ H	$J = 3/2 - 1/2 e F = 1 - 1$	32667.6366	22 (7)	4.37 (12)	0.86 (27)	20 (6)
HC ₇ N	$J = 29 - 28$	32711.6820	19 (11)	4.70 (9)	0.47 (24)	14 (6)
C ₆ H ⁻	$J = 12 - 11$	33044.4879	<16	<13
CC ³⁴ S	$N_J = 2_3 - 1_2$	33111.8390	34 (7)	4.76 (7)	0.94 (16)	37 (7)
CCS	$N_J = 2_3 - 1_2$	33751.3737	792 (45)	4.81 (1)	0.76 (1)	650 (38)
DC ₃ N	$J = 4 - 3$	33772.5312	58 (7)	4.71 (5)	1.3 (10)	80 (9)
HC ₇ N	$J = 30 - 29$	33839.6250	<19	<16
HC ₅ N	$J = 13 - 12$	34614.3870	368 (22)	4.76 (1)	0.77 (1)	301 (19)
C ₆ H	² Π _{3/2} $J = 25/2 - 23/2 f$	34654.0373	13 (6)	4.68 (22)	1.28 (48)	22 (6)
C ₆ H	² Π _{3/2} $J = 25/2 - 23/2 e$	34658.3831	14 (5)	4.71 (20)	1.39 (49)	18 (5)
C ₃ S	$J = 6 - 5$	34684.3675	247 (17)	4.70 (1)	0.76 (2)	200 (15)
C ₆ H	² Π _{1/2} $J = 27/2 - 25/2 f$	34887.1145	<18	<15
C ₆ H	² Π _{1/2} $J = 27/2 - 25/2 e$	34917.8847	<18	<15
HC ₇ N	$J = 31 - 30$	34967.5880	11 (6)	4.75 (27)	1.52 (65)	17 (5)
C ₆ H ⁻	$J = 13 - 12$	35798.1532	<17	<14 ...
C ₄ H ₂	$J_{K_a, K_c} = 4_{13} - 3_{12}$ (ortho)	35875.7746	33 (6)	4.65 (7)	1.14 (18)	41 (7)
HC ₇ N	$J_k = 3_2 - 3_1$	36095.5340	24 (12)	4.67 (7)	0.39 (17)	10 (4)
CH ₃ OH	$J_k = 4_{-1} - 3_0 E$	36169.2610	94 (10)	4.71 (2)	0.87 (5)	86 (9)
HC ₃ N	$J = 4 - 3 F = 4 - 4$	36390.8861	76 (9)	4.77 (3)	0.82 (6)	83 (9)
HC ₃ N ^a	$J = 4 - 3 \Delta F = -1$	36392.3240	1673 (90)	2158 (114)
HC ₃ N	$J = 4 - 3 F = 3 - 43$	36394.1765	83 (9)	4.74 (2)	0.74 (5)	65 (7)
HC ₇ N	$J = 33 - 32$	37223.4920	24 (7)	4.82 (9)	0.67 (20)	19 (6)
C ₄ H ⁻	$J = 4 - 3$	37239.4020	<17	<14
HC ₅ N	$J = 14 - 13$	37276.9940	264 (18)	4.77 (1)	0.79 (2)	223 (16)
C ₆ H	² Π _{3/2} $J = 27/2 - 25/2 f$	37426.1916	31 (8)	4.87 (6)	0.69 (15)	24 (5)
C ₆ H	² Π _{3/2} $J = 27/2 - 25/2 e$	37431.2550	19 (5)	4.61 (14)	1.5 (33)	32 (7)
C ₄ H	$N = 4 - 3 J = 9/2 - 7/2$	38049.6583	398 (24)	4.80 (1)	1.15 (1)	494 (32)
C ₄ H	$N = 4 - 3 J = 7/2 - 5/2$	38088.4587	385 (23)	4.78 (1)	0.93 (1)	384 (24)
CH ₃ CHO	$J_{K_a, K_c} = 2_{02} - 2_{01} E$	38505.9990	44 (6)	4.50 (5)	0.87 (11)	40 (6)
CH ₃ CHO	$J_{K_a, K_c} = 2_{02} - 2_{01} A$	38512.1130	59 (8)	4.97 (3)	0.83 (8)	55 (7)
C ₆ H ⁻	$J = 14 - 13$	38551.8083	<17	<14
DC ₃ N	$J = 5 - 4$	42215.5827	108 (17)	4.59 (5)	0.95 (12)	110 (18)
HCO ⁺	$J_{K_a, K_c} = 2_{02} - 1_{01}$	42766.1975	<51	<42
<i>t</i> -CH ₃ CH ₂ OH	$J_{K_a, K_c} = 1_{01} - 0_{00}$	43026.6000	<51	<42
DC ₃ N	$J = 17 - 16$	43215.4382	<51	<42
HNCO	$J_{K_a, K_c} = 2_{02} - 1_{01}$	43963.0000	100 (24)	4.45 (7)	0.72 (17)	81 (24)
CCS	$N_J = 4_3 - 3_2$	43981.0270	127 (30)	4.70 (5)	0.54 (11)	86 (20)
<i>c</i> -C ₃ H ₂	$J_{K_a, K_c} = 3_{21} - 3_{12}$ (ortho)	44104.7806	189 (30)	4.48 (3)	0.63 (8)	128 (21)
C ₄ D	$N = 5 - 4 J = 11/2 - 9/2$	44146.0772	<63	<52
C ₄ D	$N = 5 - 4 J = 9/2 - 7/2$	44182.0627	<63	<52
HC ₅ N	$J = 17 - 16$	45264.7199	278 (34)	4.53 (2)	0.62 (5)	193 (25)
HC ₃ N ^a	$J = 5 - 4 \Delta F = -1$	45490.3138	2198 (132)	1965 (115)
<i>c</i> -C ₃ H ₂	$J_{K_a, K_c} = 2_{11} - 2_{02}$ (para)	46755.6136	840 (63)	4.56 (1)	0.64 (2)	618 (54)
<i>t</i> -CH ₃ CH ₂ OH	$J_{K_a, K_c} = 4_{04} - 3_{13}$	46832.8000	<81	<67
C ₄ H	$N = 5 - 4 J = 11/2 - 9/2$	47566.8090	635 (54)	4.68 (1)	0.64 (3)	443 (38)
C ₄ H	$N = 5 - 4 J = 9/2 - 7/2$	47605.4850	515 (46)	4.55 (1)	0.65 (3)	380 (39)
HC ₅ N	$J = 18 - 17$	47927.2746	226 (43)	4.52 (3)	0.45 (7)	106 (21)
CH ₃ OH	$J_k = 1_0 - 0_0 A^+$	48372.4600	657 (68)	4.51 (1)	0.52 (3)	365 (37)
CS	$J = 1 - 0$	48990.9549	2465 (145)	4.44 (1)	0.91 (1)	2579 (160)
C ₃ N ^a	$N = 5 - 4 J = 11/2 - 9/2$	49466.4200	117 (42)	4.72 (9)	0.68 (24)	77 (21)
C ₃ N	$N = 5 - 4 J = 9/2 - 7/2$	49485.2480	<126	<104
<i>c</i> -C ₃ HD	$J_{K_a, K_c} = 1_{11} - 0_{00}$	49615.8517	366 (54)	4.48 (3)	0.56 (6)	222 (34)

NOTE. — Errors on the last quoted digit(s) are given in parentheses. Upper limits are $3\Delta v \times \text{RMS noise}$, with $\Delta v = 0.78$.

^a HC₃N and C₃N measurements are integrated over the three main hyperfine components.

in the plane of the sky, and indicate a gradient in the chemical/physical properties of the gas.

3.2. Molecular column densities

All spectral lines – observed at the Kontinen et al. (2000) HC₃N peak – were fitted using single Gaussians. Integrated line intensities and fit parameters are given in Table 1. One-sigma errors were calculated using Monte Carlo noise re-sampling with 1000 replications. The errors in T_{MB} and $\int T_{\text{MB}} dv$ given in the table also include uncertainties of $\pm 5\%$ to account for errors in T_{MB} introduced by the atmospheric opacity correction as a result of uncertainties in the atmospheric model parameters. Measured line FWHM are in the range 0.4 – 1.5 km s⁻¹. Unresolved hyperfine structure is present in many of the lines, and causes significant additional broadening of the observed line widths for HC₃N, C₃N, DC₃N, C₄H and C₆H. Ignoring outliers more than one standard deviation from the mean, the average line FWHM is 0.78 km s⁻¹.

Molecular column densities are presented in Table 2. These were calculated using a variety of methods as indicated in the table notes. Spectral line data and partition functions have been taken from The Cologne Database for Molecular Spectroscopy (Müller et al. 2001), with supplementary data from the JPL database⁴. Partition functions for the different nuclear spin configurations of *c*-C₃H₂ and CH₃OH were calculated by direct summation over the relevant energy levels. The beam-filling factor was assumed to be unity for all emission, which is justified based on the spatial extent of the emission maps. However, structure on size scales less than the size of the Mopra beam is likely given the presence of the compact protostellar core. This may introduce additional uncertainties into the derived column densities and temperatures.

3.2.1. Rotational diagrams

Rotational diagrams (see, *e.g.* Cummins et al. 1986) were used for those species for which at least two transitions from significantly different upper-state energies were observed. The rotational diagrams containing at least three transitions each are shown in Figure 5. Where possible, in order to better constrain the temperatures and column densities, our data were supplemented with data from the SEST observations of Kontinen et al. (2000). Derived rotational excitation temperatures T_{rot} are relatively low ($\lesssim 10$ K), so it was necessary to account for the cosmic microwave background (CMB) radiation by including a factor $[1 - (J_{\nu}(T_{\text{bg}})/J_{\nu}(T_{\text{rot}}))]^{-1}$ in the column density calculations, where $J_{\nu}(T)$ is the Planck radiation law and $T_{\text{bg}} = 2.73$ K is the CMB temperature. For HC₃N, C₄H, ortho-*c*-C₃H₂ and CCS, the peak opacities (τ_{ν}) are significant for one or more lines, so for these species the points on the rotational diagram were corrected using the factor

$$c_{\nu} = \tau_{\nu}/(1 - e^{-\tau_{\nu}}), \quad (1)$$

where τ_{ν} was derived from the opacity equation

$$T_{\text{MB}} = [J_{\nu}(T_{\text{rot}}) - J_{\nu}(T_{\text{bg}})](1 - e^{-\tau_{\nu}}) \quad (2)$$

The correction factors were determined iteratively, with initial values (c_{ν}^0) calculated at temperatures of $T_{\text{rot}}^0(\text{HC}_3\text{N}) = 7.6$ K, $T_{\text{rot}}^0(\text{C}_4\text{H}) = 4.3$ K, $T_{\text{rot}}^0(\text{ortho-}c\text{-C}_3\text{H}_2) = 7.7$ K and $T_{\text{rot}}^0(\text{CCS}) = 5.8$ K, which were derived from the respective

⁴ <http://spec.jpl.nasa.gov/>

TABLE 2
MOLECULAR COLUMN DENSITIES AND ABUNDANCES

Species	N (cm ⁻²)	T (K)	Abundance	Method ^a
C ₃ H	2.9 ^{+0.9} _{-0.5} (12)	6.1 ± 1.4	9.5 ⁺¹⁰ _{-3.6} (-11)	(1)
C ₄ H	1.4 ^{+0.8} _{-0.5} (14)	4.9 ± 1.0	4.6 ^{+6.6} _{-2.3} (-9)	(2)
C ₄ H ⁻	< 4.5 (10)	6.1 ± 1.4	< 2.4 (-12)	(1)
C ₆ H	5.9 ^{+2.9} _{-1.3} (11)	6.1 ± 1.4	2.0 ^{+2.7} _{-0.9} (-11)	(1)
C ₆ H ⁻	< 4.8 (10)	6.1 ± 1.4	< 2.5 (-12)	(1)
C ₃ N	2.5 ^{+1.6} _{-0.9} (12)	6.1 ± 1.4	8.2 ⁺¹³ _{-4.3} (-11)	(1)
HC ₃ N	2.0 (13)	7.1	6.7 (-10)	(3)
HC ₃ N	1.6 ^{+0.2} _{-0.1} (13)	7.2 ± 0.2	5.3 ^{+3.6} _{-3.8} (-10)	(4)
HC ₅ N	4.5 ^{+1.6} _{-1.2} (12)	7.1 ± 0.8	1.5 ^{+1.7} _{-0.7} (-10)	(2)
HC ₇ N	3.3 ^{+8.0} _{-1.5} (12)	6.1 ± 1.4	1.1 ^{+4.9} _{-0.7} (-10)	(1)
DC ₃ N	7.3 ^{+2.3} _{-1.1} (11)	6.1 ± 1.4	2.4 ^{+2.6} _{-0.9} (-11)	(2)
DC ₅ N	< 4.9 (12)	6.1 ± 1.4	< 2.6 (-10)	(1)
o- <i>c</i> -C ₃ H ₂	1.3 ^{+5.9} _{-0.4} (13)	6.1 ± 1.4	4.3 ⁺³¹ _{-2.0} (-10)	(3)
o- <i>c</i> -C ₃ H ₂	8.7 ^{+0.9} _{-0.8} (12)	6.6 ± 0.3	2.9 ^{+2.1} _{-0.9} (-10)	(4)
p- <i>c</i> -C ₃ H ₂	1.4 ^{+1.0} _{-0.3} (13)	6.1 ± 1.4	4.7 ^{+7.3} _{-2.0} (-10)	(3)
p- <i>c</i> -C ₃ H ₂	1.5 ^{+1.1} _{-0.4} (13)	6.1 ± 1.4	5.0 ^{+5.5} _{-1.0} (-10)	(1)
<i>c</i> -C ₃ HD	4.5 ^{+1.3} _{-0.7} (12)	6.1 ± 1.4	1.5 ^{+1.5} _{-0.6} (-10)	(1)
C ₄ H ₂ ^b	2.1 ^{+3.5} _{-1.3} (12)	6.1 ± 1.4	6.8 ⁺²³ _{-4.9} (-11)	(1)
HNCO	7.6 ^{+3.5} _{-2.3} (12)	6.1 ± 1.4	2.5 ^{+3.3} _{-1.2} (-10)	(1)
HCO ₂ ⁺	< 9.0 (11)	6.1 ± 1.4	< 4.7 (-11)	(1)
CH ₃ OH-A	6.0 ^{+1.9} _{-1.3} (12)	7.1 ± 0.9	2.0 ^{+2.1} _{-0.8} (-10)	(4)
CH ₃ OH-E	1.2 ^{+0.8} _{-0.5} (13)	4.7 ± 0.6	4.0 ^{+6.3} _{-2.1} (-10)	(4)
CH ₃ CHO	3.6 ^{+1.0} _{-0.5} (12)	6.1 ± 1.4	1.2 ^{+1.2} _{-0.4} (-10)	(1)
<i>t</i> -CH ₃ CH ₂ OH	< 1.2 (13)	6.1 ± 1.4	< 5.0 (-10)	(1)
CS	> 3.8 (13)	6.1 ± 1.4	> 9.5 (-11)	(1)
CCS	1.3 ^{+0.2} _{-0.1} (13)	5.6 ± 0.2	4.2 ^{+3.3} _{-1.5} (-10)	(4)
CC ³⁴ S	7.5 ^{+2.7} _{-1.5} (11)	6.1 ± 1.4	2.5 ^{+2.9} _{-1.0} (-11)	(1)
C ₃ S	2.3 ^{+0.9} _{-0.4} (12)	6.1 ± 1.4	7.6 ^{+2.1} _{-2.9} (-11)	(1)

NOTE. — Base-ten exponents are given in parentheses. Column density upper limits are 3σ . Abundances are given with respect to H₂ column density $(3 \pm 1) \times 10^{22}$ cm⁻².

^a Method used for column density calculation: (1) LTE with $T_{\text{rot}} = 6.1 \pm 1.4$; (2) Rotational diagram; (3) Best-fit RADEX radiative transfer model (with density set to $n_{\text{H}_2} = 10^6$ cm⁻³); (4) Rotational diagram including supplementary data from (Kontinen et al. 2000).

^b Total C₄H₂ column density calculated from ortho species assuming an equilibrium ortho-to-para ratio (3:1).

uncorrected rotational diagrams for these species. For each successive iteration, new correction factors (c_{ν}^i) were calculated based on the temperatures derived from the previous iteration. Converged rotational temperatures and corresponding column densities are given in Table 2.

3.2.2. LTE calculations

For molecules for which rotational diagrams could not be plotted, column densities were calculated under the assumption of local thermodynamic equilibrium (LTE), using a gas temperature of 6.1 ± 1.4 K, which is the mean average ($\pm 1\sigma$), of the excitation temperatures derived from the rotational diagrams.

For molecules in this category with multiple line detections, the weighted-average column densities were calculated based on the individual line signal-to-noise ratios. Where molecular lines were searched for but not detected, column density upper limits were calculated using upper integrated line inten-

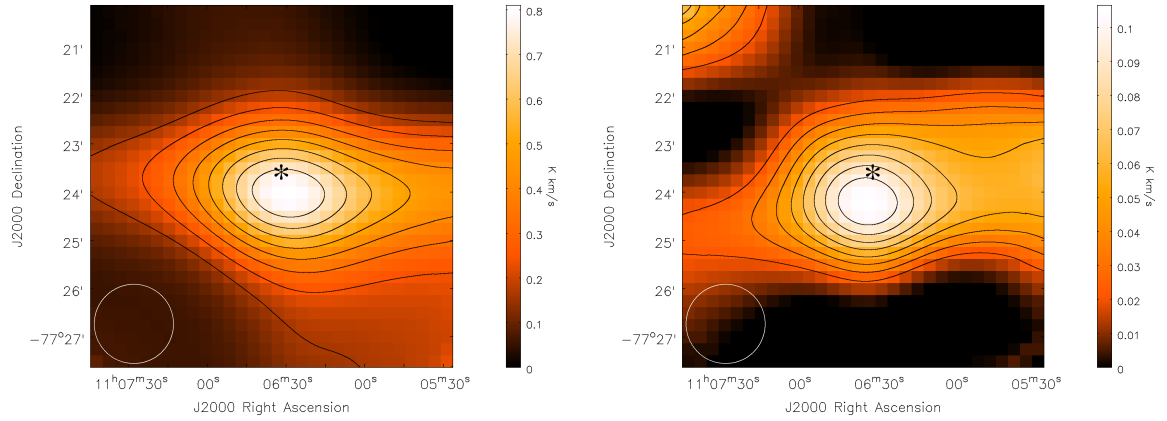


FIG. 2.— Integrated emission intensity maps of $\text{HC}_3\text{N } J = 4 - 3$ (left) and $\text{HC}_5\text{N } J = 13 - 12$ (right). The protostar Cha-MMS1 is marked with an asterisk, which denotes the center of the millimeter source. Telescope beam shown in bottom left.

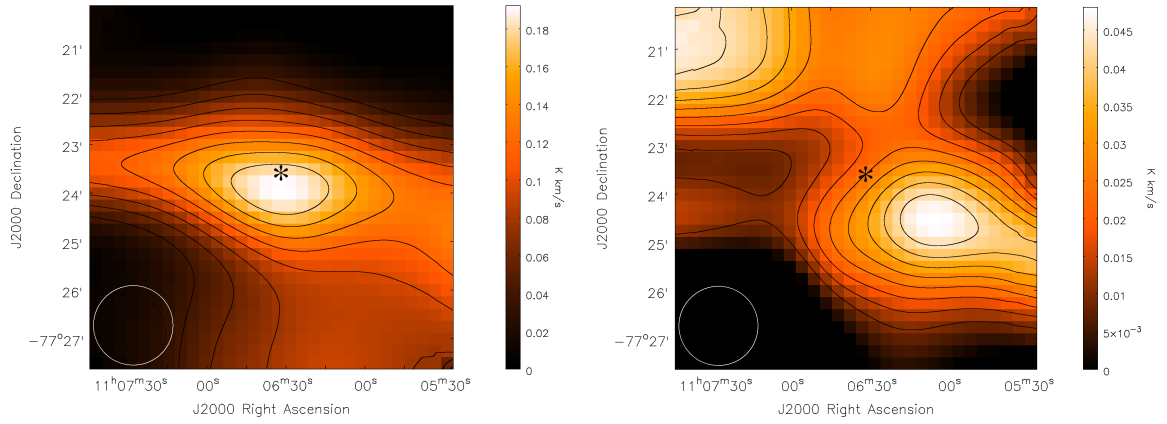


FIG. 3.— Integrated emission intensity maps of $\text{C}_4\text{H } N = 4 - 3$ (left) and $\text{CH}_3\text{OH } J_k = 4_{-1} - 3_{0\text{E}}$ (right). The protostar Cha-MMS1 is marked with an asterisk, which denotes the center of the millimeter source. Telescope beam shown in bottom left.

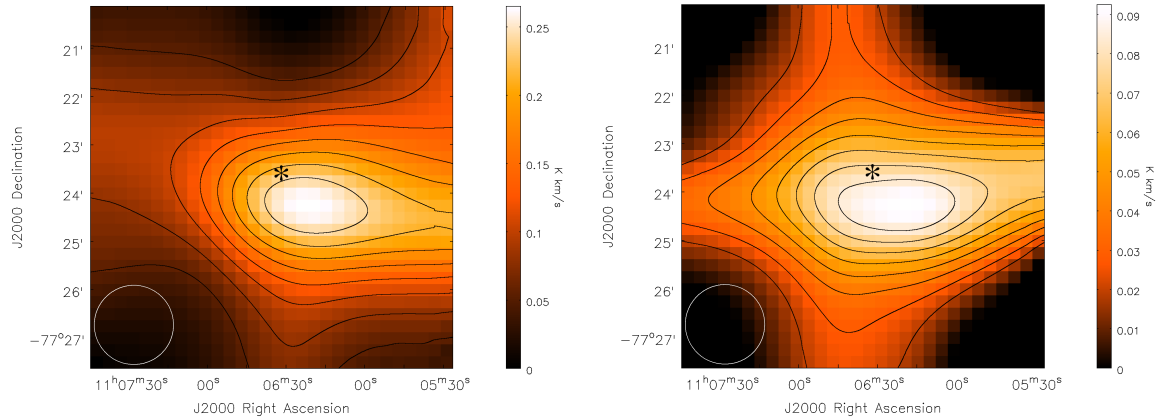


FIG. 4.— Integrated emission intensity maps of $\text{CCS } N_j = 4_3 - 3_2$ (left) and $\text{C}_3\text{S } J = 6 - 5$ (right). The protostar Cha-MMS1 is marked with an asterisk, which denotes the center of the millimeter source. Telescope beam shown in bottom left.

sity limits of $3\Delta\nu \times (\text{RMS noise})$, for which $\Delta\nu = 0.78 \text{ km s}^{-1}$ was used. For C_6H^- , the upper limit of $4.79 \times 10^{10} \text{ cm}^{-2}$ was derived from the average of the three observed C_6H^- spectra.

3.2.3. Radiative transfer modelling

For HC_3N and $c\text{-C}_3\text{H}_2$, the observed emission lines were subject to radiative transfer modelling using the RADEX code developed by van der Tak et al. (2007). This routine employs a statistical equilibrium calculation for molecular excitation involving collisional and radiative processes, and accounts for optical depth effects using an escape probability method. Collisional and radiative (de-)excitation rates were taken from the Leiden Atomic and Molecular Database (LAMDA) (Schöier et al. 2005)⁵, which tabulates scaled versions of the original data published by Green & Chapman (1978) for HC_3N and Chandra & Kegel (2000) for $c\text{-C}_3\text{H}_2$. The RADEX model free parameters (number density of primary collision partner n_{H_2} , gas kinetic temperature T and molecular column density N) were optimised using a least-squares algorithm to produce the best fit to the observed integrated line intensities (including the additional higher-frequency line data from Kontinen et al. 2000).

The two nuclear-spin species of $c\text{-C}_3\text{H}_2$ (ortho and para) were considered separately. For ortho- $c\text{-C}_3\text{H}_2$, the following transitions were included in the fitting: $J_{K_a K_c} = 2_{12} - 1_{01}$, $3_{12} - 2_{21}$ and $3_{21} - 3_{12}$. The best-fitting density was $1.0 \times 10^6 \text{ cm}^{-3}$, but T and N were not well constrained by the data. Therefore, in addition to the LTE values, RADEX column densities for ortho- and para- $c\text{-C}_3\text{H}_2$ are given in Table 2, calculated using a fixed density of $n_{\text{H}_2} = 1.0 \times 10^6 \text{ cm}^{-3}$ and temperature $T = 6.1 \pm 1.4 \text{ K}$. Even at densities $\sim 10^6$, the complexity of the $c\text{-C}_3\text{H}_2$ spectrum results in significant departures from LTE excitation, so the results from radiative transfer modelling are preferred over the LTE/rotational diagram results. However, the calculated ortho- $c\text{-C}_3\text{H}_2$ energy level populations are highly dependant on the assumed temperature, which leads to substantial uncertainty in the column density. On the other hand, the HC_3N rotational excitation is close to LTE, as shown by the near-linearity of the corrected rotational diagram in Figure 5. As a result, the gas density is only constrained by a lower limit ($n_{\text{H}_2} \gtrsim 5.5 \times 10^5 \text{ cm}^{-3}$), derived using a RADEX fit to the $J = 4-3$, $5-4$, $10-9$ and $11-10$ transitions. Above this value, the best-fitting HC_3N column density is relatively density-insensitive; the value for $N(\text{HC}_3\text{N})$ shown in Table 2 was calculated for $n_{\text{H}_2} = 1.0 \times 10^6 \text{ cm}^{-3}$. The best-fitting HC_3N excitation temperature was 7.1 K , which matches well the value of $7.2 \pm 0.2 \text{ K}$ derived from the corrected HC_3N rotational diagram.

4. DISCUSSION

4.1. Molecular column densities and abundances

Based on the dust emission, Tennekes et al. (2006) calculated an average H_2 column density of $N(\text{H}_2) = (3 \pm 1) \times 10^{22} \text{ cm}^{-2}$ in a $50''$ beam surrounding Cha-MMS1. Using this range, the observed molecular abundances relative to H_2 are given in Table 2.

Our column densities for CCS, $c\text{-C}_3\text{H}_2$, HC_3N and CH_3OH differ from those published by Kontinen et al. (2000), who used a line-ratio method for the derivation of LTE excitation temperatures. Their derived temperatures are significantly less than ours (for all species except A-methanol), lead-

ing to greater line opacities and column densities. For example, Kontinen et al. (2000) derived $T_{\text{ex}} = 4.7 \pm 0.2 \text{ K}$, $N = 4.7 \times 10^{13} \text{ cm}^{-2}$ for $c\text{-C}_3\text{H}_2$, and $T_{\text{ex}} = 4.1 \pm 0.1 \text{ K}$, $N = 4.5 \times 10^{14} \text{ cm}^{-2}$ for HC_3N . For their strongest observed lines of these species, core opacities of $\tau_{\nu} \approx 3$ were derived, whereas we derive opacities less than 1 based on their data for the same transitions. Their HC_3N column density, in particular, seems unrealistically large compared to other carbon-chain rich interstellar clouds (even the TMC-1 cyanopolyne peak); we derive values of $2.0 \times 10^{13} \text{ cm}^{-2}$ using RADEX modelling and $1.6 \times 10^{13} \text{ cm}^{-2}$ using a (corrected) rotational diagram. Their use of approximate partition functions for ortho and para $c\text{-C}_3\text{H}_2$ is another source of discrepancy.

The mean gas number density within a $\text{FWHM} = 50''$ beam surrounding Cha-MMS1 was found by Belloche et al. (2011) to be $9.8 \times 10^5 \text{ cm}^{-3}$ (assuming a dust temperature of 12 K), which closely matches our derived H_2 number density of $n_{\text{H}_2} = 1.0 \times 10^6 \text{ cm}^{-3}$. If the dust temperature is closer to our mean derived value of 6.1 K , the density calculated by Belloche et al. (2011) could be up to about a factor of 3 greater. This would still be consistent with our results however, given their smaller beam size, which probed more of the higher-density material nearer to the protostar.

4.1.1. Polyynes and cyanopolyynes

The abundances of carbon-chain-bearing species (including the polyynes and cyanopolyynes) in Cha-MMS1 are large, and similar to those found in other carbon-chain-rich interstellar clouds, prestellar cores and protostars such as TMC-1, L1527 (Sakai et al. 2008b), L1521E (Hirota et al. 2004), L1512 and L1251A (Cordiner et al. 2011).

Previous laboratory and theoretical studies have shown that polyynes and cyanopolyynes may be rapidly synthesised in cold, dark interstellar clouds through gas-phase ion-molecule and neutral-neutral chemistry (e.g. Herbst & Leung 1989; Smith et al. 2004). Large abundances of carbon-chain-bearing molecules are often taken as a sign of chemical youth in molecular clouds (e.g. Suzuki et al. 1992; Hirota et al. 2009; Takakuwa et al. 2011). Indeed, the large abundances of these species in TMC-1 can be explained as being due to the ‘early-time peak’ that occurs when reactive carbon is still freely available in the gas (before it becomes almost completely locked up in CO). In environments denser than TMC-1, gas-phase species freeze out more rapidly onto dust due to increased collision rates, and this can become an important driver of large-molecule chemistry: Assuming equal sticking probabilities for all species involved in gas-grain collisions, lighter species (including atomic oxygen) travel at higher velocities and therefore freeze out more quickly than the heavier, slower-moving carbon chains. Because O is a primary destructive reactant for carbon-chain-bearing species, their abundances rise as oxygen freezes out. This is known as the ‘freeze-out peak’ (e.g. Brown & Charnley 1990), and may be a plausible explanation for the large carbon chain abundances observed in Cha-MMS1 and other dense cores. Evidence in favour of a freeze-out-peak chemistry in Cha-MMS1 is given by the CO depletion and large NH_3 abundance (Tennekes et al. 2006).

Alternatively, Sakai et al. (2008b, 2009a) hypothesised that elevated carbon chain abundances in L1527 arise as a result of heating by the newly-formed protostar IRAS 04368+2557. Once the outer envelope reaches a temperature $\gtrsim 30 \text{ K}$, it is theorised that grain-surface methane begins to sublimate,

⁵ <http://www.strw.leidenuniv.nl/~moldata>

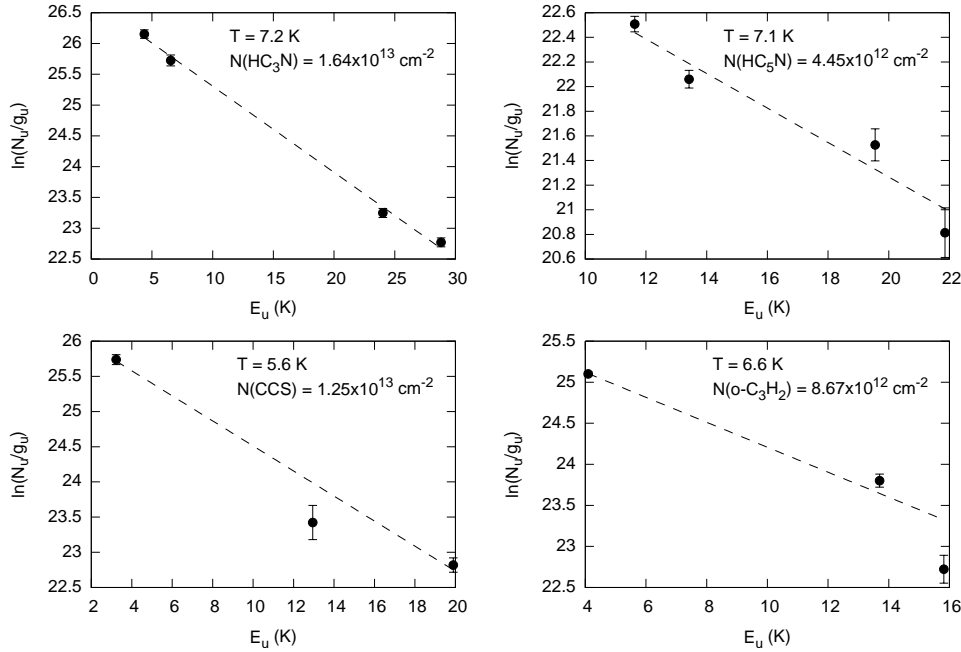


FIG. 5.— Rotational diagrams for HC_3N , HC_5N , CCS and $o\text{-}c\text{-C}_3\text{H}_2$, including data from the present work and from Kontinen et al. (2000). Lines of best fit are shown (with corresponding LTE excitation temperatures T and column densities N). Integrated line intensities have been opacity-corrected (see Section 3.2.1).

which then reacts with gas-phase C^+ to form hydrocarbon ions. These subsequently engage in ion-molecule reactions and give rise to a so-called ‘warm carbon-chain chemistry’ (WCCC). Chemical models show that this mechanism is capable of producing elevated abundances of unsaturated hydrocarbons including polyynes and cyanopolyynes in the warm regions surrounding low-mass protostars (Hassel et al. 2008). The detection of high-excitation-energy carbon chain emission lines in L1527 by Sakai et al. (2008b) is consistent with this theory. High-excitation lines have not yet been detected in Cha-MMS1, but we are presently undertaking new observations to search for them. The HC_3N $J = 10 - 9$ map of Cha-MMS1 published by Kontinen et al. (2000) shows a north-south elongation in the peak emission contour, which covers both the location of the protostar and the more southerly peak in our observed HC_3N $J = 4 - 3$ map. The $J = 4 - 3$ emission originates from a rotational energy level (E_u) only 4.3 K above the ground state, whereas the $J = 10 - 9$ emission originates from $E_u = 24$ K and therefore provides evidence for a significant contribution to the HC_3N emission from warmer, more excited gas heated by the protostar. It is possible that carbon chain abundances may be enhanced as a result of WCCC in this region. However, Kontinen et al. (2000) did not detect any emission from the high-excitation ($E_u = 52$ K) $J = 15 - 14$ line of HC_3N , which indicates that any warm and dense region must be small compared with the $37''$ SEST beam.

According to the physical model of protostar evolution by Masunaga & Inutsuka (2000), during the FHSC stage soon before the protostar begins fusion, the temperature reaches above 30 K at radial distances from the core $R_{30} \lesssim 20$ AU. The protostar subsequently ignites and warms the surrounding envelope over time. After 2×10^4 yr, R_{30} is predicted to increase to ~ 1000 AU, and increases further during the mid-to-late stages of the Class 0 phase, but by a relatively smaller amount. The Mopra beam HWHM of $\approx 40''$ corresponds to 6000 AU at the distance of Cha-MMS1, so emission from the cool, extended outer envelope of the (collapsing) protostar dominates the observed spectra, and any emission from the

compact methane-sublimation region (inside R_{30}) would be severely diluted regardless of the evolutionary state of the protostar, making the WCCC signature difficult to detect. In the case of Cha-MMS1 (with its very low luminosity), the warm region close to the protostar is probably too small to make a significant contribution to our observed emission. Our non-detection of the more highly-excited ${}^2\Pi_{1/2}$ $J = 27/2 - 25/2$ emission lines of C_6H (with $E_u = 31$ K) is not surprising given the expected beam dilution.

On the other hand, if Cha-MMS1 contains a VeLLO undergoing episodic accretion, the size of the warm (methane-sublimation) region is predicted to vary in accordance with the accretion rate (see for example, Lee 2007). Therefore, if Cha-MMS1 is presently at or near to a minimum in the accretion rate cycle, there may still be abundant carbon chains around the protostar, left over from a previous epoch of WCCC that occurred when the accretion rate and protostar luminosity were greater, and the size of R_{30} correspondingly larger. It must be emphasised, however, that the ‘cold’ carbon chain emission peaks (see Figures 2 to 4) are offset from the protostar centre, so WCCC is an unlikely explanation for the majority of the carbon-chain-rich material surrounding Cha-MMS1. Smaller telescope beam sizes combined with the observation of high excitation-energy lines to probe warmer gases will be required for further analysis of the carbon chemistry inside the putative methane sublimation zone and warm inner envelope of Cha-MMS1.

4.1.2. Anions

The polyne anions C_4H^- and C_6H^- were not detected. Three-sigma upper limits on their respective anion-to-neutral ratios are $[\text{C}_4\text{H}^-]/[\text{C}_4\text{H}] < 0.02\%$ and $[\text{C}_6\text{H}^-]/[\text{C}_6\text{H}] < 10\%$, which include the errors in the observed abundances of the neutral species. The largest anion-to-neutral ratios observed in any astronomical source so far (for both species) have been in L1527 where $[\text{C}_4\text{H}^-]/[\text{C}_4\text{H}] = 0.01\%$ (Agúndez et al. 2008) and $[\text{C}_6\text{H}^-]/[\text{C}_6\text{H}] = 9\%$ (Sakai et al. 2008c), which are consistent with our results.

In chemical models for dense clouds (*e.g.* Millar et al. 2007; Harada & Herbst 2008), the observed C_6H^- anion-to-neutral ratios (on the order of a few percent) are reproduced with good accuracy. However, our non-detection of C_4H^- provides a new example of the observed C_4H anion-to-neutral ratio being substantially less than predicted by theory (see Herbst & Osamura 2008).

4.1.3. Methanol

Methanol is found in the gas phase in dense molecular clouds, prestellar cores and in the vicinity of protostars, with column densities $\sim 10^{13} - 10^{15} \text{ cm}^{-2}$ (*e.g.* Friberg et al. 1988; Maret et al. 2005; Buckle et al. 2006). However, most of the methanol in cold, dense protostellar envelopes is found in the form of ice (Boogert et al. 2008). Its formation *via* gas-phase chemistry is inefficient (Geppert et al. 2006), and methanol is widely believed to be formed by successive hydrogenation of CO on cold dust grain surfaces. Its appearance in the gas phase in cold regions has been hypothesised to be due to cosmic-ray-induced desorption, reactive desorption, or heating in grain-grain collisions, whereas inside protostellar envelopes, heating of the material to temperatures $\geq 100 \text{ K}$ results in complete evaporation of the ices (*e.g.* Rodgers & Charnley 2003).

The CH_3OH map in Figure 3 does not rule out the existence of methanol in warm gas in the vicinity of the protostar, but similar to the carbon-chain-bearing species, the fact that the emission peak is offset by $\sim 10^4 \text{ AU}$ shows that protostellar heating probably does not explain the majority of the observed methanol. The lack of spatial correlation between the CH_3OH and carbon chain distributions matches the observations made by Buckle et al. (2006), who used chemical models to infer the physical and chemical histories of HC_3N -rich and CH_3OH -rich gas clumps. The observed methanol peak offset in Cha-MMS1 is consistent with the theory presented by Markwick et al. (2000) and Buckle et al. (2006), that Alfvén waves emitted by nearby collapsing protostars cause transient removal of ice mantles from the surrounding dust, resulting in the liberation of methanol into the gas phase at a distance from the protostellar core on the order of the MHD-wave damping length ($\sim 10^4 \text{ AU}$). Markwick et al. (2000) used this theory to successfully explain the origin of the abundance gradients of various species observed along the ridge of TMC-1. The young age of Cha-MMS1 implies that protostellar collapse is currently in progress, resulting in the production of Alfvén waves that could be responsible for desorption of the observed methanol.

From the ratios of our observed CH_3OH lines with those of Kontinen et al. (2000), differing temperatures were calculated for the A and E methanol nuclear spin species of $7.1 \pm 0.9 \text{ K}$ and $4.7 \pm 0.6 \text{ K}$, respectively. The column densities of A and E methanol (given in Table 2) also differ, but within the error bars. The ratio of the sums over the statistical weights of the quantum states of A and E methanol approaches unity, so in the limit of high temperature (in thermodynamic and chemical equilibrium), the abundances of A and E methanol should be approximately equal. Convergence of the A and E abundances is calculated to occur for temperatures above about 30 K (see Wirström 2009; Wirström et al. 2011). At lower temperatures, A-methanol is the more abundant species because its ground state is 7.9 K lower in energy than that of E-methanol. Given that both spin species are likely to have the same spatial distribution in the ISM, their relative column densities in Cha-MMS1 may be more accurately compared by assuming a

common excitation temperature. In LTE at 6.1 K, the column densities of A and E methanol calculated from our observations are $(7.2 \pm 0.7) \times 10^{12} \text{ cm}^{-2}$ and $(6.6 \pm 0.7) \times 10^{12} \text{ cm}^{-2}$. Using only the higher-frequency lines observed by Kontinen et al. (2000), we calculate the respective column densities to be $(7.5 \pm 0.7) \times 10^{12} \text{ cm}^{-2}$ and $(7.9 \pm 0.8) \times 10^{12} \text{ cm}^{-2}$. These results are consistent with equal abundances of A and E methanol, implying formation at close to statistical equilibrium.

4.1.4. Deuterium fractionation

In cold interstellar clouds, molecular ions become enriched in deuterium as a result of exothermic gas-phase fractionation reactions involving HD (Millar et al. 1989).

Belloche et al. (2006) found a deuterated N_2H^+ fraction in Cha-MMS1 of $[N_2D^+]/[N_2H^+] = 11\%$, which is typical for prestellar cores and young protostars observed in the nearby Galaxy. The cyanoacetylene deuteration fraction $[DC_3N]/[HC_3N] = 3.6 \pm 1.5\%$ is within the range of values previously observed in TMC-1 (1 – 6%; Turner 2001; Saito et al. 2002), and is similar to the carbon-chain-rich prestellar core L1544 (6%; Howe et al. 1994), and the protostar L1527 (3%; Sakai et al. 2009b). These results are consistent with chemical models for cold interstellar clouds (*e.g.* Roberts & Millar 2000; Turner 2001; Pagani et al. 2009).

4.1.5. Cyclopropenylidene

A large *c*- C_3HD column density of $4.5^{+1.3}_{-0.7} \times 10^{12} \text{ cm}^{-2}$ is found in Cha-MMS1, which is about 5 times greater than in L1527 and an order of magnitude greater than in TMC-1 (Sakai et al. 2009b; Turner 2001). Accounting for the rather large uncertainty in the *c*- C_3H_2 column density (see Section 3.2.3), we calculate that the cyclopropenylidene deuteration fraction $[c-C_3HD]/[c-C_3H_2]$ is between 5% and 34%. This is not significantly different from the range of values (5 – 15%) reported in a sample of twelve dark clouds by Bell et al. (1988), and the value of 7% reported in L1527 by Sakai et al. (2009b), but is consistent with previous results which show the *c*- C_3H_2 deuteration fraction is larger than that of HC_3N (*e.g.* Turner 2001; Sakai et al. 2009b). Chemical models predict comparable levels of deuteration for *c*- C_3HD and HC_3N ; deuterium enrichment in both these species is considered to originate predominantly from the CH_2D^+ ion (*e.g.* Roberts & Millar 2000; Turner 2001). Deuteration may also occur by deuteron transfer as a result of collisions with H_2D^+ , followed by dehydrogenation upon recombination. Discrepancy between the deuteration fractions of *c*- C_3HD and HC_3N is indicative of an incomplete understanding of the deuterium chemistry of these two species. The fact that *c*- C_3H_2 can become doubly deuterated may partly explain why *c*- C_3HD is so abundant: if sufficient *c*- C_3D_2 forms, it would act as a buffer for *c*- C_3HD in subsequent proton-deuteron exchange processes. It may thus be of interest to search for *c*- C_3D_2 in Cha-MMS1 and similar environments. However, we are not aware of any published laboratory studies on the rotational spectrum of *c*- C_3D_2 ; such a study would be warranted.

The *c*- C_3H_2 molecule exists in two nuclear spin configurations: ortho and para, and it has been suggested that the ortho-to-para ratio (OPR) may be used as a probe of interstellar cloud ages (Morisawa et al. 2006). However, our present data are insufficient to usefully constrain the OPR. Additional observations of *c*- C_3H_2 and *c*- C_3HD lines from a range of energy levels and with a range of optical depths will be

required in order to better constrain the column densities of these species and derive more reliable values for the $c\text{-C}_3\text{H}_2$ OPR and deuteration fraction.

4.1.6. Sulphuretted species

We observed large abundances of the sulphur-bearing carbon chains C_nS ($n = 1-3$), on the same order of magnitude as found in various parts of the Taurus molecular cloud complex (*e.g.* Hirota et al. 2004). Our $[\text{CCS}]/[\text{C}_3\text{S}]$ column density ratio (5.7 ± 2.1) is greater than the values observed by Hirota et al., of 2.1, 2.3, 2.0 in the dense cores L1495B, L1521B and L1521E, respectively, and is more similar to the value of 5.1 found in TMC-1. The relatively large value in Cha-MMS1 is primarily attributable to a relatively low C_3S column density, which is more consistent with the lower C_3S column densities observed in the carbon-chain-rich cloud cores L1512 and L1251A by Cordiner et al. (2011).

Sulphur is believed to be incorporated into gas-phase hydrocarbon molecules in the ISM mainly by ion-neutral chemistry involving S^+ (Millar & Herbst 1990). Recombination of HC_nS^+ species then produces sulphuretted carbon chains. The main source of HC_3S^+ is from the reaction $\text{S}^+ + c\text{-C}_3\text{H}_2 \rightarrow \text{HC}_3\text{S}^+ + \text{H}$, followed by recombination of HC_3S^+ to produce C_3S . Thus, the relatively low C_3S abundance in Cha-MMS1 could be explained by a relative underabundance of $c\text{-C}_3\text{H}_2$ compared with L1495B, L1521B and L1521E. An alternative method for the synthesis of C_3S is by the neutral-neutral reaction $\text{C}_2\text{H} + \text{CS} \rightarrow \text{C}_3\text{S} + \text{H}$ (Smith et al. 2004). However, this reaction is relatively slow (two orders of magnitude slower than the ion-neutral reaction), and is therefore expected to be less important in the production of C_3S .

The $[\text{N}_2\text{H}^+]/[\text{CCS}]$ ratio may be used as a measure of chemical age in interstellar clouds on the basis that carbon chains are most abundant at early times, whereas N_2H^+ becomes more abundant later on as CO freezes out (*e.g.* Takakuwa et al. 2011). Using the N_2H^+ abundance from Belloche et al. (2006), we derive $[\text{N}_2\text{H}^+]/[\text{CCS}] = 0.5 \pm 0.3$ in Cha-MMS1, which is similar to the value of 0.52 ± 0.07 found in the young, carbon-chain-rich VeLLO L1521F (Takakuwa et al. 2011), indicating a comparable chemical age, but less than the value 1.18 ± 0.21 in the more evolved VeLLO IRAM 04191.

Only a lower limit could be placed on the CS column density because the optical depth of the $J = 1-0$ lines approaches infinity for the adopted temperature range of 6.1 ± 1.4 K.

4.1.7. Other molecules

Acetaldehyde (CH_3CHO) was detected in Cha-MMS1 with a column density of $3.6 \times 10^{12} \text{ cm}^{-2}$. It is an important molecule in terrestrial organic chemistry, and has been detected in star-forming regions, protostars and translucent/dense molecular clouds. A range of gas and ice-phase reaction pathways have been proposed to explain its abundance in space (see Charnley 2004; Bennett et al. 2005, and references therein). However, the size of the Mopra beam does not place any useful constraint on the origin of the emission relative to the protostar, and therefore, apart from highlighting the diversity of the organic chemistry of this region, the observed CH_3CHO abundance of $\approx 10^{-10}$ does not significantly constrain the physics or chemistry of the molecule or the protostar. Our observations are, however, consistent with equal abundances of gas-phase A- and E- CH_3CHO , indicating statistical equilibrium.

Ethanol ($\text{CH}_3\text{CH}_2\text{OH}$) has previously been observed with relatively large abundances of $\sim 10^{-8}$ in ‘hot core’ regions

surrounding high-mass protostars (*e.g.* Millar et al. 1995), but is not present in quiescent (non-star-forming) molecular clouds. There have been two reported detections to-date in low-mass protostars: an abundance of $\sim 10^{-8}$ was found in the hot corino IRAS 16293-2422A by Huang et al. (2005) and $\sim 10^{-7}$ in the L1157 outflow by Arce et al. (2008). We derive a (beam-averaged) upper limit on the ethanol abundance of 5×10^{-10} in Cha-MMS1.

We also searched for the protonated carbon dioxide ion HCO_2^+ and derive an upper abundance limit of 4.7×10^{-11} . This molecule was detected by Sakai et al. (2008a) in the vicinity of the low-mass protostar L1527, with a beam-averaged abundance of 1.3×10^{-12} . HCO_2^+ is believed to be formed predominantly by protonation of CO_2 , and the gas-phase CO_2 abundance can be estimated using Equation 5 of Sakai et al. (2008a). Using a CO abundance of 5×10^{-5} (calculated using the C^{18}O column density of $2.5 \times 10^{15} \text{ cm}^{-2}$ reported by Kontinen et al. 2000 and an intrinsic $^{16}\text{O}/^{18}\text{O}$ ratio of 500), we derive an upper limit of $n(\text{CO}_2) < 4 \times 10^{-6} n_{\text{H}_2}$, averaged over the Mopra beam. Spitzer observations (Furlan et al. 2008) show a solid CO_2 abundance of 5×10^{-6} towards L1527 and a similar ice abundance may be expected in the cool, outer envelope of Cha-MMS1. The relatively low gas-phase CO_2 in Cha-MMS1 implied by our observations, combined with the upper limit on the ethanol abundance, shows that the energetic processing of matter that would cause the sublimation of dust grain mantles in the protostellar envelope, due to heating by the protostar or an outflow shock, for example, must be lacking in Cha-MMS1, or at least confined to a relatively small area compared with the $\approx 90''$ Mopra beam.

4.2. Comparison with other sources

The molecular abundances in Cha-MMS1 are indicative of an active (non-equilibrium) carbon chemistry, resulting in the synthesis of large quantities of unsaturated carbon-chain-bearing species such as the polyynes and cyanopolyynes. The carbon-chain abundances are similar to those in young, quiescent cores such as TMC-1 and the ‘carbon-chain-producing regions’ observed by Suzuki et al. (1992) and Hirota et al. (2004, 2009). However, as pointed out by Tennekes et al. (2006), the CO depletion and large NH_3 abundance in Cha-MMS1 are hallmarks of a later stage of chemical evolution, associated with the freezing-out of gas-phase species onto the dust, as has been observed in prestellar cores and the outer envelopes of other young, low-to-intermediate-mass protostars (Caselli et al. 1999; Jørgensen et al. 2004; Crapsi et al. 2005; Alonso-Albi et al. 2010).

Only a few detections of long carbon-chain-bearing species in low-mass protostellar envelopes have been reported to-date. The smaller species HC_3N , C_3H_2 and C_4H in Cha-MMS1 are a factor of a few to an order of magnitude more abundant than those surrounding the VeLLO L1521F and the prestellar core L1544 (see Suzuki et al. 1992; Gupta et al. 2009; Takakuwa et al. 2011), both of which are considered to be relatively carbon-chain-rich sources. Due to their evolved state, the appearance of carbon-chain-bearing molecules in these sources is likely to be the result of ‘freeze-out-peak’ chemistry (see Section 4.1.1).

Carbon chains have also been hypothesised to arise in large abundances in protostellar envelopes as a result of warm carbon-chain chemistry (WCCC) (Sakai et al. 2009a). Of all the dense molecular clouds in the literature for which multiple complex molecules have been observed, the abundances in

Cha-MMS1 match most closely with those in the well-studied Class 0/I protostar L1527 in the Taurus molecular cloud complex (Sakai et al. 2008b, 2009a,b), where WCCC has been theorised to be occurring. Indeed, the abundances of all observed species in Cha-MMS1 are within an order of magnitude of those observed in L1527.

The gas densities in the envelopes of Cha-MMS1 and L1527 are quite similar ($\sim 10^6 \text{ cm}^{-3}$), so the similarities in their chemistries may be related to similarities in the physical conditions. It is tempting, therefore, to hypothesise that the large abundances of organic molecules around Cha-MMS1 also arise as a result of WCCC. However, Cha-MMS1 is likely to be at a significantly earlier stage of evolution than L1527, and has an estimated luminosity $\sim 1/100$ as large (Jørgensen et al. 2002; Belloche et al. 2011). The low IR flux and lack of outflow from the protostar (Belloche et al. 2006; Hiramatsu et al. 2007) indicate that Cha-MMS1 is very close to the beginning of the Class 0 phase, whereas L1527 is more evolved, with bright scattered IR emission and clear outflow cavities, consistent with an edge-on Class I protostar obscured by its own disk (Tobin et al. 2008). Assuming a uniform accretion rate, Ohashi et al. (1997) calculated the age of the L1527 protostar to be $\sim 10^5$ yr, which would place it at the end of the Class 0 phase (based the Class 0 lifetime derived by Enoch et al. 2009). Chemical timescales in dense interstellar clouds (in particular, molecular freeze-out timescales; see Equation 4 of Buckle et al. 2006) are significantly less than the estimated $\sim 10^5$ yr age difference of these two protostars. Therefore, the chemical similarity between Cha-MMS1 and L1527 may be coincidental. Notwithstanding the possibility of episodic outbursts, the low luminosity of Cha-MMS1 implies a very small hot-core region (probably $\lesssim 10$ AU in size), that would not be detectable with single-dish microwave telescopes. Instead, the large carbon chain abundances observed in the envelope of Cha-MMS1 may be present because this young protostar is forming from a very chemically-rich parent molecular cloud.

Crapsi et al. (2005) derived CO depletion factors $\delta_{\text{CO}} \sim 10$ in L1521F and L1544. Using the CO abundance from Section 4.1.7, we calculate $\delta_{\text{CO}} \sim 2$ in Cha-MMS1 (assuming an undepleted CO abundance of 9.5×10^{-5} after Crapsi et al. 2005). The size of the warm region around the Cha-MMS1 protostar within which CO ice is desorbed is likely to be negligible compared with the telescope beam, so low CO depletion may be a sign that the freezing-out of gas-phase species onto the dust is less far advanced. This would be consistent with a relatively short prestellar phase for Cha-MMS1. Alternatively, the low CO depletion could be a consequence of grain mantle destruction; significant turbulent motion of the gas around Cha-MMS1 may be inferred from the relatively broad molecular linewidths ($\approx 0.78 \text{ km s}^{-1}$), which are more than an order of magnitude greater than the thermal limit in most cases, and are significantly broader than observed in L1521F ($< 0.3 \text{ km s}^{-1}$; Gupta et al. 2009). This may be a signature of energetic cloud motions that cause collisions between dust grains, resulting in the liberation of mantle species into the gas phase. Possible physical processes responsible for mantle destruction include inter-clump collisions or Alfvén waves emitted by the protostar. As discussed in Section 4.1.3, the liberation of mantle species may explain the origin of the observed methanol. According to Markwick et al. (2000), grain mantle desorption also gives rise to large gas-phase abundances of polyynes and cyanopolyynes.

To help ascertain the origin of complex molecules in the

vicinity of Cha-MMS1, direct observations of the core region at higher spatial resolution are required, which will also help to establish the precise physical nature of the source and identify molecular signatures of the earliest stages of star formation. For example, observations of the gas-phase products of grain-surface chemistry (in particular, alcohols, saturated organic molecules and deuterated species) will probe the presence of a possible hot corino (*e.g.* Cazaux et al. 2003). High-resolution maps will permit the search for molecular abundance gradients due to Alfvén waves predicted by Markwick et al. (2000). The identification of concentrated abundances of carbon chains around the protostar would provide evidence for warm carbon chain chemistry (Sakai et al. 2010). Lee (2007) theorised that by mapping the N_2H^+ and CO abundances at high angular resolution, and using infrared CO_2 ice observations in the protostellar envelope, it should be possible to observe the chemical effects of the episodic accretion process hypothesised to be present in VeLLOs. Omukai (2007) calculated that high-excitation submillimeter H_2O emission lines may be used as a tracer for the presence of the infall shock-front that is predicted to be a characteristic property of first hydrostatic cores. A compact, low-velocity outflow is predicted to be another characteristic of the FHSC phase (Machida et al. 2008; Tomida et al. 2010). It may thus be possible to determine whether Cha-MMS1 is a VeLLO or an FHSC using high angular-resolution ($\sim 0.1 - 1''$) molecular line observations.

5. CONCLUSION

The envelope of the low-luminosity protostar Cha-MMS1 exhibits an unusually rich chemical diversity. It contains very large abundances of organic molecules, indicative of active gas-phase and grain-surface chemical processes near to the protostar. The abundances of long carbon chains (including C_6H and HC_7N) are particularly large, and similar to those found in the most carbon-chain-rich regions of the Galaxy. These observations show that complex organic molecules and carbon-chain-bearing species can be abundant in star-forming gas, and may therefore be of relevance to studies of the chemical evolution of protoplanetary disks. The molecular abundances in Cha-MMS1 are similar to those in the envelope of the older, more luminous Class 0/I protostar L1527, and are greater than have been reported so far for any other low-luminosity, low-mass Class 0 protostellar envelope (including the VeLLOs L1521F, L1014 and IRAM 04191). This may be attributable to a combination of factors including (1) a young chemical age for the Cha-MMS1 natal interstellar cloud, (2) freezing out of atomic oxygen onto the dust, and (3) the liberation of grain mantle species into the gas by various mechanisms such as clump-clump collisions, Alfvén waves or warming by the protostar.

The observations presented here are of lines from relatively low excitation levels which trace predominantly cool material; the chemistry of the warmer regions closer to the protostar may be examined by the observation of higher-excitation lines at higher spatial resolution. This will permit further analysis of the relationship between protostar and envelope chemistry. Establishing the molecular inventory of the envelope of Cha-MMS1 and other young protostars will be of fundamental importance towards the goal of understanding the initial chemical reagents available for the formation of planetary systems.

We gratefully acknowledge the assistance of Balt Inder-

muehle at Mopra for providing support during on-site and remote observations. Thanks to Arnaud Belloche for comments on the manuscript. This work was supported by the Goddard

Center for Astrobiology and NASA's Origins of Solar Systems and Exobiology programs.

Facilities: Mopra

REFERENCES

- Agúndez, M., Cernicharo, J., Guélin, M., et al. 2008, *A&A*, 478, L19
- Alonso-Albi, T., Fuente, A., Crimier, N., et al. 2010, *A&A*, 518, A52+
- Arce, H. G., Santiago-García, J., Jørgensen, J. K., Tafalla, M., & Bachiller, R. 2008, *ApJ*, 681, L21
- Barnes, D. G., Staveley-Smith, L., de Blok, W. J. G., et al. 2001, *MNRAS*, 322, 486
- Bell, M. B., Avery, L. W., Matthews, H. E., et al. 1988, *ApJ*, 326, 924
- Belloche, A., Parise, B., van der Tak, F. F. S., et al. 2006, *A&A*, 454, L51
- Belloche, A., Schuller, F., Parise, B., et al. 2011, *A&A*, 527, A145+
- Bennett, C. J., Osamura, Y., Lebar, M. D., & Kaiser, R. I. 2005, *ApJ*, 634, 698
- Boogert, A. C. A., Pontoppidan, K. M., Knez, C., et al. 2008, *ApJ*, 678, 985
- Boss, A. P. & Yorke, H. W. 1995, *ApJ*, 439, L55
- Brown, P. D. & Charnley, S. B. 1990, *MNRAS*, 244, 432
- Buckle, J. V., Rodgers, S. D., Wirstrom, E. S., et al. 2006, *Faraday Discussions*, Vol. 133, p. 63-82, 133, 63
- Caselli, P., Walmsley, C. M., Tafalla, M., Dore, L., & Myers, P. C. 1999, *ApJ*, 523, L165
- Cazaux, S., Tielens, A. G. G. M., Ceccarelli, C., et al. 2003, *ApJ*, 593, L51
- Cernicharo, J., Guélin, M., & Askne, J. 1984, *A&A*, 138, 371
- Chandra, S. & Kegel, W. H. 2000, *A&AS*, 142, 113
- Charnley, S. B. 2004, *Advances in Space Research*, 33, 23
- Charnley, S. B. & Rodgers, S. D. 2008, *Space Sci. Rev.*, 138, 59
- Charnley, S. B. & Rodgers, S. D. 2009, in *Advances in Geosciences*, Volume 15: Planetary Science (PS), ed. A. Bhardwaj, Vol. 15, 211–+
- Chen, X., Arce, H. G., Zhang, Q., et al. 2010, *ApJ*, 715, 1344
- Cordiner, M. A., Charnley, S. B., Buckle, J. V., Walsh, C., & Millar, T. J. 2011, *ApJ*, 730, L18+
- Crapsi, A., Caselli, P., Walmsley, C. M., et al. 2005, *ApJ*, 619, 379
- Cummins, S. E., Linke, R. A., & Thaddeus, P. 1986, *ApJS*, 60, 819
- Dunham, M. M., Crapsi, A., Evans, II, N. J., et al. 2008, *ApJS*, 179, 249
- Ehrenfreund, P. & Charnley, S. B. 2000, *ARA&A*, 38, 427
- Enoch, M. L., Evans, N. J., Sargent, A. I., & Glenn, J. 2009, *ApJ*, 692, 973
- Enoch, M. L., Lee, J., Harvey, P., Dunham, M. M., & Schnee, S. 2010, *ApJ*, 722, L33
- Friberg, P., Hjalmarson, A., Madden, S. C., & Irvine, W. M. 1988, *A&A*, 195, 281
- Furlan, E., McClure, M., Calvet, N., et al. 2008, *ApJS*, 176, 184
- Geppert, W. D., Hamburger, M., Thomas, R. D., et al. 2006, *Faraday Discussions*, 133, 177
- Green, S. & Chapman, S. 1978, *ApJS*, 37, 169
- Gupta, H., Gottlieb, C. A., McCarthy, M. C., & Thaddeus, P. 2009, *ApJ*, 691, 1494
- Harada, N. & Herbst, E. 2008, *ApJ*, 685, 272
- Hassel, G. E., Herbst, E., & Garrod, R. T. 2008, *ApJ*, 681, 1385
- Herbst, E. & Leung, C. M. 1989, *ApJS*, 69, 271
- Herbst, E. & Osamura, Y. 2008, *ApJ*, 679, 1670
- Herbst, E. & van Dishoeck, E. F. 2009, *ARA&A*, 47, 427
- Hiramatsu, M., Hayakawa, T., Tatematsu, K., et al. 2007, *ApJ*, 664, 964
- Hirota, T., Maezawa, H., & Yamamoto, S. 2004, *ApJ*, 617, 399
- Hirota, T., Ohishi, M., & Yamamoto, S. 2009, *ApJ*, 699, 585
- Howe, D. A., Millar, T. J., Schilke, P., & Walmsley, C. M. 1994, *MNRAS*, 267, 59
- Huang, H.-C., Kuan, Y.-J., Charnley, S. B., et al. 2005, *Advances in Space Research*, 36, 146
- Jørgensen, J. K., Schöier, F. L., & van Dishoeck, E. F. 2002, *A&A*, 389, 908
- Jørgensen, J. K., Schöier, F. L., & van Dishoeck, E. F. 2004, *A&A*, 416, 603
- Knude, J. & Hog, E. 1998, *A&A*, 338, 897
- Kontinen, S., Harju, J., Heikkilä, A., & Haikala, L. K. 2000, *A&A*, 361, 704
- Larson, R. B. 1969, *MNRAS*, 145, 271
- Lee, J. 2007, *Journal of Korean Astronomical Society*, 40, 85
- Machida, M. N., Inutsuka, S.-i., & Matsumoto, T. 2008, *ApJ*, 676, 1088
- Maret, S., Ceccarelli, C., Tielens, A. G. G. M., et al. 2005, *A&A*, 442, 527
- Markwick, A. J., Millar, T. J., & Charnley, S. B. 2000, *ApJ*, 535, 256
- Masunaga, H. & Inutsuka, S. 2000, *ApJ*, 536, 406
- Meier, R., Owen, T. C., Jewitt, D. C., et al. 1998, *Science*, 279, 1707
- Millar, T. J., Bennett, A., & Herbst, E. 1989, *ApJ*, 340, 906
- Millar, T. J. & Herbst, E. 1990, *A&A*, 231, 466
- Millar, T. J., MacDonald, G. H., & Habing, R. J. 1995, *MNRAS*, 273, 25
- Millar, T. J., Walsh, C., Cordiner, M. A., Ní Chuimín, R., & Herbst, E. 2007, *ApJ*, 662, L87
- Morisawa, Y., Fushitani, M., Kato, Y., et al. 2006, *ApJ*, 642, 954
- Müller, H. S. P., Thorwirth, S., Roth, D. A., & Winnewisser, G. 2001, *A&A*, 370, L49
- Mumma, M. J. & Charnley, S. B. 2011, *Annu. Rev. Astron. Astrophys.*, in press
- Ohashi, N., Hayashi, M., Ho, P. T. P., & Momose, M. 1997, *ApJ*, 475, 211
- Omukai, K. 2007, *PASJ*, 59, 589
- Pagani, L., Vastel, C., Hugo, E., et al. 2009, *A&A*, 494, 623
- Pineda, J. E., Arce, H. G., Schnee, S., et al. 2011, in press
- Reipurth, B., Nyman, L., & Chini, R. 1996, *A&A*, 314, 258
- Roberts, H. & Millar, T. J. 2000, *A&A*, 361, 388
- Rodgers, S. D. & Charnley, S. B. 2003, *ApJ*, 585, 355
- Saito, S., Aikawa, Y., Herbst, E., et al. 2002, *ApJ*, 569, 836
- Sakai, N., Sakai, T., Aikawa, Y., & Yamamoto, S. 2008a, *ApJ*, 675, L89
- Sakai, N., Sakai, T., Hirota, T., Burton, M., & Yamamoto, S. 2009a, *ApJ*, 697, 769
- Sakai, N., Sakai, T., Hirota, T., & Yamamoto, S. 2008b, *ApJ*, 672, 371
- Sakai, N., Sakai, T., Hirota, T., & Yamamoto, S. 2009b, *ApJ*, 702, 1025
- Sakai, N., Sakai, T., Hirota, T., & Yamamoto, S. 2010, *ApJ*, 722, 1633
- Sakai, N., Sakai, T., & Yamamoto, S. 2008c, *ApJ*, 673, L71
- Schöier, F. L., van der Tak, F. F. S., van Dishoeck, E. F., & Black, J. H. 2005, *A&A*, 432, 369
- Smith, I. W. M., Herbst, E., & Chang, Q. 2004, *MNRAS*, 350, 323
- Suzuki, H., Yamamoto, S., Ohishi, M., et al. 1992, *ApJ*, 392, 551
- Takakuwa, S., Ohashi, N., & Aikawa, Y. 2011, *ApJ*, 728, 101
- Tennekes, P. P., Harju, J., Juvela, M., & Tóth, L. V. 2006, *A&A*, 456, 1037
- Tobin, J. J., Hartmann, L., Calvet, N., & D'Alessio, P. 2008, *ApJ*, 679, 1364
- Tomida, K., Tomisaka, K., Matsumoto, T., et al. 2010, *ApJ*, 714, L58
- Turner, B. E. 2001, *ApJS*, 136, 579
- van der Tak, F. F. S., Black, J. H., Schöier, F. L., Jansen, D. J., & van Dishoeck, E. F. 2007, *A&A*, 468, 627
- Willacy, K. 2007, *ApJ*, 660, 441
- Wirstrom, E. S., Geppert, W. D., Hjalmarson, A., et al. 2011, *A&A*, in press
- Wirstrom, E. S. 2009, PhD thesis, Onsala Space Observatory, S-43992 Onsala, Sweden